

Manifold Random Features

Ananya Parashar ^{* 1} Derek Long ^{* 1} Dwaipayan Saha ^{* 1} Krzysztof Choromanski ^{* † 1,2}

^{*}Equal contribution [†]Senior lead

Abstract

We present a new paradigm for creating random features to approximate bi-variate functions (in particular, kernels) defined on general manifolds. This new mechanism of *Manifold Random Features* (MRFs) leverages discretization of the manifold and the recently introduced technique of *Graph Random Features* (GRFs; (Choromanski, 2023)) to learn continuous fields on manifolds. Those fields are used to find continuous approximation mechanisms that otherwise, in general scenarios, cannot be derived analytically. MRFs provide positive and bounded features, a key property for accurate, low-variance approximation. We show deep asymptotic connection between GRFs, defined on discrete graph objects, and continuous random features used for regular kernels. As a by-product of our method, we re-discover recently introduced mechanism of Gaussian kernel approximation applied in particular to improve linear-attention Transformers, considering simple random walks on graphs and by-passing original complex mathematical computations. We complement our algorithm with a rigorous theoretical analysis and verify in thorough experimental studies.

1. Introduction & Related Work

Random features (RFs) (Rahimi & Recht, 2007; 2008; Le et al., 2013; Yang et al., 2014; Pham & Pagh, 2025; Liu et al., 2022; Choromanski et al., 2022; Likhosherstov et al., 2023; Choromanski et al., 2017; 2019; Rowland et al., 2018; Yu et al., 2016)) provide powerful techniques for translating potentially highly non-linear bi-variate functions into a simple dot-product (linear) kernel via randomized nonlinear transformations $\phi : \mathbb{R}^d \rightarrow \mathbb{R}^m$ applied separately to two input vectors. Thus RFs lead to effective mappings between non-linear methods in the original spaces and well-understood

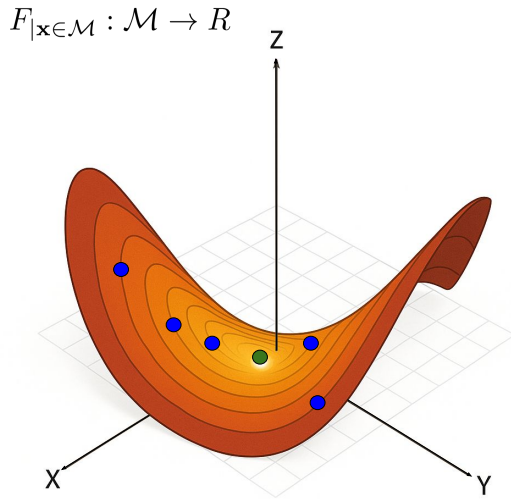


Figure 1. An illustration of the heat kernel $F : \mathcal{M} \times \mathcal{M} \rightarrow \mathbb{R}$ defined on the saddle-like surface \mathcal{M} with a distinguished point $x \in \mathcal{M}$ marked green. The values $F(x, y)$ for different $y \in \mathcal{M}$ are color-coded (different shades of red), with a couple of samples y highlighted as blue dots. For a general manifold, F is given by a system of partial differential equations and neither it nor the corresponding RF-mechanism are given by the closed-form expressions.

and computationally more efficient linear methods in the ϕ -transformed spaces. Examples range from classic algorithms such as SVM (Huang et al., 2014; Sun et al., 2018) to feedforward fully-connected architectures (Sehanobish et al., 2024; Kim et al., 2024) and attention techniques in Transformers (Choromanski et al., 2021; Likhosherstov et al., 2021; Peng et al., 2021; Nguyen et al., 2024; Sun et al., 2025; Zhang et al., 2024).

Constructing efficient mappings $\phi_1, \phi_2 : \mathbb{R}^d \rightarrow \mathbb{R}^m$ (in many applications, a symmetric setting $\phi_1 = \phi_2 = \phi$ is considered, but a priori it is not a strict requirement) to approximate given bi-variate function $F : \mathbb{R}^d \times \mathbb{R}^d \rightarrow \mathbb{R}$ (with error $\epsilon \rightarrow 0$ as $m, d \rightarrow \infty$, often unbiasedly), as:

$$F(\mathbf{x}, \mathbf{y}) \approx \phi_1(\mathbf{x})^\top \phi_2(\mathbf{y}), \quad (1)$$

is a nontrivial task, even for the well-known kernel-functions, which are some of the most natural targets of

¹Columbia University ²Google DeepMind. Correspondence to: Ananya Parashar <ap4658@columbia.edu>.

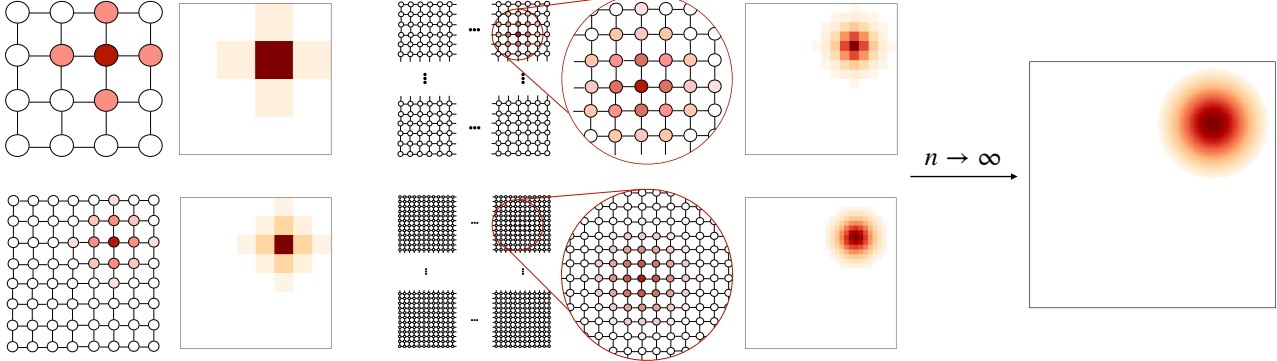


Figure 2. Four grid-graphs of sizes: 4×4 , 8×8 , 16×16 , 32×32 with the distinguished vertex \mathbf{z} and its corresponding *signature vectors* obtained by applying GRF algorithm (Choromanski, 2023). The signature vectors are represented by color-coding different vertices (with more intense shades corresponding to large values and the most intense used to color vertex \mathbf{z}). Next to the graphs, those signature vectors are also represented by color-coding unit-squares. As the resolution of the grid goes to infinity, those representations converge to the continuous object, namely function g_i from Eq. 2.

the RF-methods. For example, a standard method applying trigonometric random features to approximate Gaussian and softmax kernels, proposed in (Rahimi & Recht, 2007), in practice does not work well in linear-attention Transformers, since it can produce negative features for the kernel that is strictly positive. The so-called *positive random features* from (Choromanski et al., 2021) address this challenge, but further refinements (e.g. the boundedness of the RFs) are needed to improve approximation quality (see: (Likhosherstov et al., 2022)). The problem becomes even more challenging when bi-variate functions F are defined on non-Euclidean spaces, e.g. on manifolds (see: Fig. 1).

In the Euclidean setting, a standard approach to constructing mappings ϕ_1, ϕ_2 is by re-writing function $F : \mathbb{R}^d \times \mathbb{R}^d \rightarrow \mathbb{R}$ as follows for some $g_1, g_2 \in \mathbb{R}^d \times \mathbb{R}^d \rightarrow \mathbb{R}$:

$$F(\mathbf{x}, \mathbf{y}) = \int_{\mathbb{R}^d} g_1(\mathbf{x}, \omega) g_2(\mathbf{y}, \omega) d\omega. \quad (2)$$

Given a probabilistic distribution $P \in \mathcal{P}(\mathbb{R}^d)$ with the corresponding density function $p : \mathbb{R}^d \rightarrow \mathbb{R}_{\geq 0}$, mappings $\phi_1, \phi_2 : \mathbb{R}^d \rightarrow \mathbb{R}^m$ can be then defined as follows for $i \in \{1, 2\}$:

$$\phi_i(\mathbf{z}) = \frac{1}{\sqrt{m}} \left(\frac{g_i(\mathbf{z}, \omega_1)}{\sqrt{p(\omega_1)}}, \dots, \frac{g_i(\mathbf{z}, \omega_m)}{\sqrt{p(\omega_m)}} \right), \quad (3)$$

where $\omega_1, \dots, \omega_m \sim P$. It is easy to see that the following holds: $F(\mathbf{x}, \mathbf{y}) = \mathbb{E}[\phi_1(\mathbf{x})^\top \phi_2(\mathbf{y})]$. It is assumed that $p(\omega) > 0$ for all $\omega \in \mathbb{R}^d$. If one wants to approximate F only on a set: $\mathcal{B}_F \times \mathcal{B}_F$ for some bounded \mathcal{B}_F , then in practice one can consider only ‘‘truncated’’ distributions \mathcal{P} with p defined only on some (sufficiently large) bounded \mathcal{B}_p , such that $|\int_{\mathbb{R}^d \setminus \mathcal{B}_p} g_1(\mathbf{x}, \omega) g_2(\mathbf{y}, \omega) d\omega|$ is sufficiently small. Finding the representations given by Eq. 2 is usually a nontrivial task and generalizations to non-Euclidean spaces are even more challenging.

In this paper, we present a new paradigm for creating random features to approximate bi-variate functions (e.g. positive-definite kernels) defined on general manifolds. This new mechanism of *Manifold Random Features* (MRFs) leverages discretization of the manifold and the recently introduced technique of *Graph Random Features* (GRFs; (Choromanski, 2023; Reid et al., 2024b; Zhang et al., 2025; Choromanski et al., 2025; Reid et al., 2024a)) to learn continuous fields on manifolds, corresponding to functions g_i from Eq. 2, but in the general (not necessarily Euclidean) setting. It turns out that these fields can be thought of as continuous extensions of the combinatorial objects, the so-called *signature vectors*, the building blocks of the GRF mechanism (see Figure 2). They are used to find continuous approximation mechanisms that otherwise, in general scenarios, cannot be derived analytically. MRFs provide positive and bounded features, a key property for accurate, low-variance approximation. We show deep asymptotic connection between GRFs, defined on discrete graph objects, and continuous random features used for regular kernels. As a by-product of our method, we rediscover recently introduced mechanism of Gaussian kernel approximation (Likhosherstov et al., 2022) applied in particular to improve linear-attention Transformers, considering simple random walks on graphs and by-passing original complex computations. We complement our algorithm with a rigorous theoretical analysis and verify it in thorough experimental studies.

2. Manifold Random Features

2.1. Preliminaries: Graph Random Features

MRFs are obtained by training continuous random feature mechanisms via discrete supervision given by *Graph Random Features* (GRFs). Thus our first step is to provide below

Algorithm 1 Regular GRFs: Construct vectors $\phi_f(i) \in \mathbb{R}^N$ to approximate $\mathbf{K}_\alpha(\mathbf{W})$

Input: weighted adjacency matrix $\mathbf{W} \in \mathbb{R}^{N \times N}$, vector of unweighted node degrees (number of out-neighbours) $\deg \in \mathbb{R}^N$, modulation function $f : (\mathbb{N} \cup \{0\}) \rightarrow \mathbb{R}$, termination probability $p_{\text{halt}} \in (0, 1)$, node $i \in \mathcal{N}$, number of random walks to sample $m \in \mathbb{N}$.

Output: signature vector $\phi_f(i) \in \mathbb{R}^N$.

```

1: initialize:  $\phi_f(i) \leftarrow \mathbf{0}$ 
2: for  $w = 1, \dots, m$  do
3:   initialize:  $\text{load} \leftarrow 1$ ,  $\text{current\_node} \leftarrow i$ ,  $\text{terminated} \leftarrow \text{False}$ ,  $\text{walk\_length} \leftarrow 0$ 
4:   while  $\text{terminated} = \text{False}$  do
5:      $\phi_f(i)[\text{current\_node}] \leftarrow \phi_f(i)[\text{current\_node}] + \text{load} \times f(\text{walk\_length})$ 
6:      $\text{walk\_length} \leftarrow \text{walk\_length} + 1$ 
7:      $\text{new\_node} \leftarrow \text{Unif}[\mathcal{N}(\text{current\_node})]$                                 ▷ assign to one of neighbours
8:      $\text{load} \leftarrow \text{load} \times \frac{\deg[\text{current\_node}]}{1-p_{\text{halt}}} \times \mathbf{W}[\text{current\_node}, \text{new\_node}]$       ▷ update load
9:      $\text{current\_node} \leftarrow \text{new\_node}$ 
10:     $\text{terminated} \leftarrow (t \sim \text{False}(0, 1) < p_{\text{halt}})$                                 ▷ draw RV  $t$  to decide on termination
11:   end while
12: end for
13: normalize:  $\phi_f(i) \leftarrow \phi_f(i)/m$ 

```

a gentle introduction to GRFs.

We will consider weighted, undirected N -vertex graphs $G(V, E, \mathbf{W} = [w(i, j)]_{i, j \in V})$, where (1) V is a set of vertices, (2) $E \subseteq V \times V$ is a set of undirected edges ($(i, j) \in E$ indicates that there is an edge between i and j in G), and (3) $\mathbf{W} \in \mathbb{R}_{\geq 0}^{N \times N}$ is a weighted adjacency matrix (no-edges encoded by zeros).

We consider the following kernel matrix $\mathbf{K}_\alpha(\mathbf{W}) \in \mathbb{R}^{N \times N}$, where $\alpha = (\alpha_k)_{k=0}^\infty$ and $\alpha_k \in \mathbb{R}$:

$$\mathbf{K}_\alpha(\mathbf{W}) = \sum_{k=0}^{\infty} \alpha_k \mathbf{W}^k. \quad (4)$$

For bounded $(\alpha_k)_{k=0}^\infty$ and $\|\mathbf{W}\|_\infty$ small enough, the above sum converges. The matrix $\mathbf{K}_\alpha(\mathbf{W})$ defines a kernel on the nodes of the graph. Importantly, Eq. 4 covers as special cases several classes of graph kernels, in particular *graph diffusion/heat kernels*, that will play an important role in our analysis later (see: Sec. 2.2.1).

GRFs provide a way to express $\mathbf{K}_\alpha(\mathbf{W})$ (in expectation) as $\mathbf{K}_\alpha(\mathbf{W}) \stackrel{\mathbb{E}}{=} \mathbf{K}_1 \mathbf{K}_2^\top$, for independently sampled $\mathbf{K}_1, \mathbf{K}_2 \in \mathbb{R}^{N \times d}$ and some $d \leq N$. This factorization gives an efficient (sub-quadratic) and unbiased approximation of the matrix-vector products $\mathbf{K}_\alpha(\mathbf{W})\mathbf{x}$ as $\mathbf{K}_1(\mathbf{K}_2^\top \mathbf{x})$, if $\mathbf{K}_1, \mathbf{K}_2$ are sparse or $d = o(N)$. This is often the case in practice. If this does not hold, explicitly materializing $\mathbf{K}_1 \mathbf{K}_2^\top$ enables one to approximate $\mathbf{K}_\alpha(\mathbf{W})$ in quadratic (versus cubic) time. Next, we describe the base GRF method for constructing sparse $\mathbf{K}_1, \mathbf{K}_2$ for $d = N$. Extensions for $d = o(N)$, using the Johnson-Lindenstrauss Transform (Dasgupta & Gupta, 2003), can be found in (Choromanski, 2023). Each

\mathbf{K}_j for $j \in \{1, 2\}$ is obtained by row-wise stacking of the vectors $\phi_f(i) \in \mathbb{R}^N$ for $i \in V$, where $f : \mathbb{R} \rightarrow \mathbb{R}$ is the graph-kernel specific *modulation function*. The procedure to construct random vectors $\phi_f(i)$ is given in Algorithm 1. Intuitively, one samples an ensemble of random walks (RWs) from each node $i \in V$. Every time a RW visits a node, the scalar value in that node is updated by the renormalized *load*, a scalar stored by each walker, updated during each vertex-to-vertex transition. The renormalization is encoded by the *modulation function*.

After all the walks terminate, the vector $\phi_f(i)$ is obtained by the concatenation of all the scalars from the discrete scalar field, followed by a simple renormalization. For unbiased estimation, $f : \mathbb{N} \rightarrow \mathbb{C}$ needs to satisfy $\sum_{p=0}^k f(k-p)f(p) = \alpha_k$, for $k = 0, 1, \dots$ (see Theorem 2.1 in (Reid et al., 2024b)). We conclude that modulation function f is obtained by deconvolving sequence $\alpha = (\alpha_k)_{k=0}^\infty$ defining graph kernel.

2.2. Constructing MRFs

For a given Riemannian manifold \mathcal{M} , and a bi-variate function $F : \mathcal{M} \times \mathcal{M} \rightarrow \mathbb{R}$, we are looking for the function $\phi_{\mathcal{M}, F} : \mathcal{M} \rightarrow \mathbb{R}^m$, such that for $x, y \in \mathcal{M}$:

$$F(x, y) \approx \phi_{\mathcal{M}, F}(x)^\top \phi_{\mathcal{M}, F}(y). \quad (5)$$

We refer to $\phi_{\mathcal{M}, F}(z)$ as a *manifold random features vector* for z . We are ready to explain how MRFs are constructed. We start with the pre-processing procedure, conducted only once for a given manifold \mathcal{M} , before inputs z_1, \dots, z_m (for which vectors $\phi_{\mathcal{M}, F}(z_i)$ need to be computed) are even known. The procedure consists of the following two steps:

Discretizations of the input manifold \mathcal{M} : We choose a resolution parameter $N \in \mathbb{N}$. We then choose a finite set of points $V_N = \{x_1, \dots, x_N\} \subset \mathcal{M}$ that discretizes \mathcal{M} ; for example, V_N can arise from a mesh, a quasi-uniform point cloud, or samples from the Riemannian volume measure. We equip V_N with a weighted neighborhood graph $G_N = (V_N, E_N, \mathbf{W}_N)$ that encodes the local geometry of \mathcal{M} , for instance by connecting each x_i to its k nearest neighbors with weights $\mathbf{W}_N(i, j) = \exp(-\|x_i - x_j\|^2/\sigma^2)$. We then consider a discretized version $F^{\text{disc}} : V_N \times V_N \rightarrow \mathbb{R}$ of the original bi-variate function $F : \mathcal{M} \times \mathcal{M} \rightarrow \mathbb{R}$, with the matrix $\mathbf{F} = [F(x_i, x_j)]_{i,j=1,\dots,N}$ adhering to the form from Eq. 4. In the most general setting, F^{disc} can be found by a regular regression algorithm trained on the dataset $\mathcal{D} = \{x_i, F(x_i)\}_{i=1}^N$ to learn a finite sequence of coefficients $(\alpha_0, \dots, \alpha_K)$ for some $K > 0$. However in lots of prominent cases of bi-variate functions defined on manifolds, this is not necessary. For instance, for the diffusion/heat kernels F defined on manifolds, the corresponding F^{disc} are the diffusion/heat kernels on the corresponding graphs G_N , with the coefficients α_k described by a closed-form formula. We describe this prominent special case in more depth in Sec. 2.2.1.

Training g -functions on manifolds: We start this phase by constructing a training dataset $\mathcal{T} = \{(x, \omega, \phi_f(x)[\omega])\}$, where $x, \omega \in V_N$ and $\phi_f(x)[\omega]$ stands for the value of the signature vector $\phi_f(x)$ in node ω . In practice, \mathcal{T} does not need to include the full N^2 set of pairs $(x, \omega) \in V_n \times V_n$ since diffusion-type kernels decay rapidly between far-apart nodes and signature vectors corresponding to neighboring nodes are similar. The signature vectors $\{\phi_f(x)\}_{x \in V_N}$ are computed with the use of Algorithm 1 (the GRF method). We construct \mathcal{T} to train a function $g_{\theta}^{\mathcal{M}, F} : \mathcal{M} \times \mathcal{M} \rightarrow \mathbb{R}_{\geq 0}$, parameterized by θ and satisfying:

$$F(x, y) \approx \int_{\mathcal{M}} g_{\theta}^{\mathcal{M}, F}(x, \omega) g_{\theta}^{\mathcal{M}, F}(y, \omega) d\omega. \quad (6)$$

Note that $g_{\theta}^{\mathcal{M}, F}$ is the generalization of the g -functions from Eq. 2. We model it as a neural network.

We train $g_{\theta}^{\mathcal{M}, F}$ to regress the discrete signature vectors on $V_N \times V_N$, and clamp the final output of $g_{\theta}^{\mathcal{M}, F}$ at zero. We define the following objective to minimize (where \mathcal{L} is a $\mathbb{R}^m \times \mathbb{R}^m \rightarrow \mathbb{R}$ loss function, e.g. L_2 -loss):

$$\min_{\theta} \frac{1}{|\mathcal{T}|} \sum_{(x, \omega, \phi_f(x)[\omega]) \in \mathcal{T}} \mathcal{L}(g_{\theta}^{\mathcal{M}, F}(x, \omega), \phi_f(x)[\omega]).$$

After training, $g_{\theta}^{\mathcal{M}, F}$ provides a smooth surrogate for discrete signatures: for $x, \omega \in V_N$, $g_{\theta}^{\mathcal{M}, F}(x, \omega) \approx \phi_f(x)(\omega)$. That completes pre-processing.

Inference: Trained $g_{\theta}^{\mathcal{M}, F}$ provides a way to approximate

$F(x, y)$ for any $x, y \in \mathcal{M}$ as follows:

$$F(x, y) \approx \sum_{\omega \in V_N} g_{\theta}^{\mathcal{M}, F}(x, \omega) g_{\theta}^{\mathcal{M}, F}(y, \omega). \quad (7)$$

This directly leads to the following definition of $\phi_{\mathcal{M}, F}$:

$$\phi_{\mathcal{M}, F}(z) = \frac{1}{\sqrt{m\kappa}} \left(\frac{g_{\theta}^{\mathcal{M}, F}(z, \omega_1)}{\sqrt{p(\omega_1)}}, \dots, \frac{g_{\theta}^{\mathcal{M}, F}(z, \omega_m)}{\sqrt{p(\omega_m)}} \right), \quad (8)$$

where either: (1) $p \equiv 1$, $m = N$, $\kappa = \frac{1}{m}$, $\{\omega_1, \dots, \omega_m\} = V_N$ or: (2) p is the density function of the probability distribution $\mathcal{P}(V_N)$ on V_N , $\kappa = 1$ and $\omega_1, \dots, \omega_m \stackrel{\text{iid}}{\sim} \mathcal{P}(V_N)$. The latter variant leads to an unbiased estimation of the sum from Eq. 7 (which is exactly what the former variant is designed to compute). It provides m -dimensional RF-vectors, instead of N -dimensional and thus can be used for dimensionality reduction.

2.2.1. DIFFUSION/HEAT KERNELS

Let (\mathcal{M}, g) be a compact d -dimensional Riemannian manifold and let $\Delta_{\mathcal{M}}$ be its Laplace–Beltrami operator (Solomon et al., 2014). The diffusion/heat kernel on \mathcal{M} is defined as follows, for a given parameter $t > 0$:

$$K_t^{\text{heat}}(x, y) = \exp(t\Delta_{\mathcal{M}})(x, y), \quad x, y \in \mathcal{M}.$$

Let \mathbf{L}_N denote the corresponding (rescaled) random-walk graph Laplacian on the discretized \mathcal{M} (corresponding to the graph $G_N = (V_N = \{x_1, \dots, x_N\}, E_N, \mathbf{W}_N)$), chosen so that \mathbf{L}_N converges to $-\Delta_{\mathcal{M}}$ in the limit, as $N \rightarrow \infty$. The discrete graph diffusion/heat kernel at time $t > 0$ is defined as follows:

$$K_{N,t}^{\text{heat}}(x_i, x_j) := [\exp(-t\mathbf{L}_N)](i, j). \quad (9)$$

It converges pointwise to the manifold heat kernel K_t^{heat} as the discretization is refined. It is easy to see that $K_{N,t}^{\text{heat}}$ adheres to the form from Eq. 4.

The class of manifold heat kernels provides a good insight into challenges related to using those constructs in machine learning that this paper addresses.

Let (\mathcal{M}, g) be a compact d -dimensional Riemannian manifold. Since \mathcal{M} is compact, the Laplace–Beltrami operator $-\Delta_{\mathcal{M}}$ has a discrete, nonnegative spectrum

$$0 = \lambda_0 \leq \lambda_1 \leq \lambda_2 \leq \dots \uparrow \infty,$$

with the corresponding orthonormal eigenfunctions $\{\phi_k\}_{k=0}^{\infty} \subset L^2(\mathcal{M})$ satisfying $-\Delta_{\mathcal{M}}\phi_k = \lambda_k\phi_k$. The heat kernel then admits the following expansion:

$$K_t^{\text{heat}}(x, y) = \sum_{k=0}^{\infty} e^{-\lambda_k t} \phi_k(x) \phi_k(y), \quad t > 0. \quad (10)$$

This expansion converges absolutely and uniformly for any $t > 0$ on compact manifolds. For reference of this result, see Theorem 10.13 of (Grigor'yan, 2009).

A naive approach to computing $K_t^{\text{heat}}(x, y)$ is via the truncation of the infinite series from Eq. 10. For a discretization $\{x_1, \dots, x_N\} \subset \mathcal{M}$, one can numerically approximate the first M eigenpairs of $-\Delta_{\mathcal{M}}$ —or of a consistent graph Laplacian approximation \mathbf{L}_N —and build the truncated kernel:

$$\widehat{K}_t^{\text{heat}}(x, y) := \sum_{k=0}^{M-1} e^{-\lambda_k t} \phi_k(x) \phi_k(y), \quad (11)$$

which converges to (10) as $M \rightarrow \infty$. Thus even for this well-studied class of manifold bi-variate functions, the (approximate) computation of the kernel matrix $\mathbf{K}_t^{\text{heat}} = [K_t^{\text{heat}}(x_i, x_j)]_{i,j=1,\dots,N} \in \mathbb{R}^{N \times N}$ requires nontrivial spectral calculations of time complexity cubic in N . Furthermore, as it is the case in general for kernel methods not leveraging RFs, downstream applications (involving multiplications with matrices $\mathbf{K}_t^{\text{heat}}$ or taking their inverses) require time $\Omega(N^2)$. In contrast, RF-based methods require sub-quadratic time (e.g. linear or log-linear for multiplications with kernel matrices, see: (Choromanski & Sindhwani, 2016)).

Note: For particularly symmetric manifolds \mathcal{M} , such as 2-dimensional spheres in \mathbb{R}^3 , there exist more explicit formulae for $K_t^{\text{heat}}(x, y)$ (see: Appendix A.3), but they still require spectral computations.

2.3. The curious case of the Gaussian kernel

MRFs are designed to efficiently apply bi-variate functions defined in non-Euclidean spaces. However, as a by-product of the presented methods, quite unexpectedly, we also obtain RF-methods for approximating regular Gaussian kernels defined in the Euclidean spaces, that were only recently introduced. We do it by applying GRFs on grid-graphs. We do think that this result is of independent interest, since it shows how combinatorial tools can lead to purely continuous ML constructions. We provide more details here.

Consider the following setting in the d -dimensional space: the Euclidean hypercube $[0, 1]^d$ equipped with the Gaussian (RBF) kernel of the following form:

$$K_{\sigma}^{\text{Gauss}}(\mathbf{x}, \mathbf{y}) = \exp\left(-\frac{\|\mathbf{x} - \mathbf{y}\|^2}{2\sigma^2}\right), \quad (12)$$

for a fixed $\sigma > 0$ and $x, y \in [0, 1]^d$. We discretize $[0, 1]^d$ with the grid of n rows/columns (so that $N = n^d$):

$$V_n := \left\{(k_1/n, \dots, k_d/n) : k_j \in \{0, \dots, n-1\}\right\}, \quad (13)$$

and side length $h_n := 1/n$. We connect each grid point to its $2d$ nearest neighbors using wrap-around at the boundary,

obtaining a d -dimensional discrete grid graph with vertex set V_n . Let \mathbf{L}_n denote the rescaled random-walk graph Laplacian on this graph, constructed as in Theorem A.1, so that \mathbf{L}_n converges to the continuous Laplacian $-\Delta$ on the discrete grid with wrap-around (the negated Laplace-Beltrami operator) in the limit $n \rightarrow \infty$. Take kernel $K_{N,t}^{\text{heat}}$ from Eq. 9 for $t = \frac{\sigma^2}{2}$. As discussed in Sec. 2.2.1, $K_{N,t}^{\text{heat}}$ converges pointwise to the heat kernel on $[0, 1]^d$, which turns out to be the Gaussian kernel $K_{\sigma}^{\text{Gauss}}$ (to be more specific, $K_{N,t}^{\text{heat}}$ converges to the periodized Gaussian kernel; in the non-periodic Euclidean limit this reduces to the standard Gaussian kernel $K_{\sigma}^{\text{Gauss}}$, see: Theorem A.2).

For each grid point $x \in V_n$ we now construct a signature vector $\phi_f(x) \in \mathbb{R}_{\geq 0}^{V_n}$ corresponding to kernel $K_{N,t}^{\text{heat}}$, as in Algorithm 1. Those signature vectors are intrinsically related to the g -functions in the representations of Gaussian kernels applied in new RF-mechanisms to approximate them. By applying techniques from (Likhosherstov et al., 2022), we obtain the following positive and bounded features representation (for completeness, we also provide a proof, see: Theorem A.3):

$$K_{\sigma}^{\text{Gauss}}(\mathbf{x}, \mathbf{y}) = \int_{\mathbb{R}^d} g_{\sigma}(\mathbf{x}, \omega) g_{\sigma}(\mathbf{y}, \omega) d\omega, \quad (14)$$

$$g_{\sigma}(\mathbf{x}, \omega) := \left(\frac{2}{\pi\sigma^2}\right)^{d/4} \exp\left(-\frac{\|\mathbf{x} - \omega\|^2}{\sigma^2}\right). \quad (15)$$

To relate the discrete signature vectors $\phi_f(x)$ to the continuous features $g_{\sigma}(\mathbf{x}, *)$, we interpret the sum over $\omega \in V_n$ as a Riemann approximation of the integral in the expression above. We show in Section 3.1 after multiplying by the grid-dependent constant $c_{d,\sigma,n} := (2\pi\sigma^2)^{d/4} n^{d/2}$, the rescaled vectors $\psi_f(x) := c_{d,\sigma,n} \cdot \phi_f(x)$ converge to $g_{\sigma}(\mathbf{x}, \omega)$ evaluated on the grid points, as $n \rightarrow \infty$. Equivalently, for any $\mathbf{x}, \mathbf{y} \in [0, 1]^d$ and the corresponding $x, y \in V_n$ of the grid-graph, we have:

$$\lim_{n \rightarrow \infty} \langle \psi_f(x), \psi_f(y) \rangle = K_{\sigma}^{\text{Gauss}}(\mathbf{x}, \mathbf{y}). \quad (16)$$

We conclude that the signature vectors on increasingly refined grids realize manifold random features for the Gaussian kernel on the corresponding continuous cube.

3. Experiments

We validate MRFs in several scenarios. As a warm-up, in Sec. 3.1 we consider the Euclidean setting with Gaussian kernels (see: Sec. 2.3). Then we transition to non-Euclidean spaces, the main target of MRFs. In Sec. 3.2, we test MRFs on various pre-defined 2D surfaces in the 3-dimensional spaces. Finally, in Sec. 3.3, we provide downstream tests for interpolation on meshes (representing rigid and deformable objects).

3.1. MRFs for Gaussian Kernels

Following the discussion in Sec. 2.3, for each dimension $d \in \{2, 4, \dots, 32\}$, we discretize the hypercube $[0, 1]^d$ via the regular grid V_n with spacing $h_n = 1/n$ and n^d nodes, connecting each node to its $2d$ wrap-around nearest neighbors. For each choice of n and d , we construct signature vectors $\phi_f(x)$ at every grid node $x \in V_n$ using the random walk procedure of Algorithm 1 with a fixed diffusion scale $\sigma = 0.2$, termination probability $p_{\text{halt}} = 0.005$, $m = 100,000$ walks per node, and vary n from 5 to 105 in steps of 10. We then form rescaled vectors $\psi_f(x) = c_{d, \sigma, n} \phi_f(x)$.

Note: On the (d -dimensional grid) V_n , the random-walk Laplacian decomposes as a Kronecker sum of 1D operators. Hence, the corresponding terms $e^{-tL/2}$ and the induced kernel e^{-tL} factorize across coordinates; see Prop. 20 (Cadaid et al., 2022) for further details. We exploit this to compute the 1D quantities and tensorize to obtain the d -dimensional results.

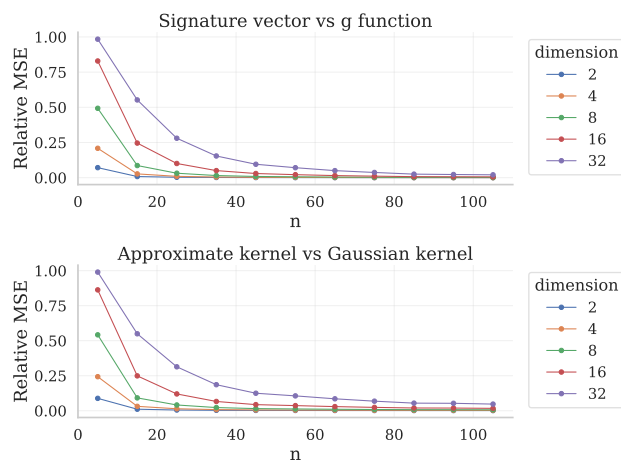


Figure 3. Empirical relative mean squared errors (MSEs) of the approximations of g -functions and true Gaussian kernel values with signature vectors and kernels induced by them for $d \in \{2, 4, \dots, 32\}$ and $n = 5, 15, \dots, 105$. Relative MSE of the approximation of vector \mathbf{y} with random vector \mathbf{x} is defined as $\mathbb{E}[\|\mathbf{x} - \mathbf{y}\|_2^2 / \|\mathbf{y}\|_2^2]$. We use $s = 30$ repetitions for each n value (the standard deviations are very small compared to the mean so not visible on the figure).

We compute the relative mean squared error (MSE) of approximating $g_\sigma(\mathbf{c}, *)$ with $\psi_f(\mathbf{c})[*]$, as well as that of approximating true kernel values with those induced by MRFs (in the grid points). The latter are given as:

$$\hat{K}_{\sigma, n}^{\text{Gauss}}(x, y) := \langle \psi_f(x), \psi_f(y) \rangle, \quad x, y \in V_n. \quad (17)$$

Across all tested dimensions, we observe that these errors decrease rapidly as the grid is refined (see: Fig. 3).

3.2. 2D Surfaces in 3D Spaces & Speed Tests

We evaluate the approximation of g -functions and diffusion/heat kernels with MRFs on four embedded non-linear geometries: a sphere, an ellipsoid, a Möbius strip, and a torus (or donut; detailed results for this shape are in the Appendix: Sec. A.6.1). For each geometry, we discretize the surface into $N = 4000$ points, build a k NN graph (with $k = 24$ for the Möbius strip and $k = 8$ for the other three), generate signature feature vectors from 1000 (sampled) start points with parameters: $m = 100,000$ (number of random walks), $p_{\text{halt}} = 0.01$, and $\sigma^2 = 20$. We then train a neural network predictor $g_\theta(\mathbf{x}, \omega)$ to learn $\phi_f(x)[\omega]$. Our network architecture is a small multilayer perceptron that takes as input the coordinates of the pair (\mathbf{x}, ω) along with an approximation of the geodesic distance $d_M(\mathbf{x}, \omega)$, (computed via a shortest path calculation between x and ω), and outputs the signature-vector values. Training was run for 1000 epochs with an absolute relative error loss (clamped at $\varepsilon = 0.1$), defined as follows:

$$\mathcal{L}(g_\theta(\mathbf{x}, \omega), \phi_f(x)(\omega)) = \frac{|g_\theta(\mathbf{x}, \omega) - \phi_f(x)(\omega)|}{\max\{\phi_f(x)(\omega), \varepsilon\}}, \quad (18)$$

and optimized with Adam. We report root mean square error (RMSE), validation diagnostics (prediction vs. actual and error vs. truth; those in the Appendix: Sec. A.6.2), qualitative 3D visualizations of $g_\theta(\mathbf{x}, \cdot)$, $\phi_f(x)[\cdot]$, and their difference for representative validation starts, and heat-kernel comparisons using the kernel induced by the learned features. From the learned feature matrix \mathbf{G}_θ we form $\mathbf{K}_\theta = \mathbf{G}_\theta \mathbf{G}_\theta^\top$, and compare it against the ground-truth kernel matrix \mathbf{K}_{GT} . Before reporting kernel errors, we apply the Frobenius-norm alignment (see: Appendix, Sec. A.5) and evaluate the renormalized version $\tilde{\mathbf{K}}_\theta$.

Sphere: We embed a sphere $x^2 + y^2 + z^2 = 1$ in \mathbb{R}^3 . For the ground truth, we use the analytic spherical heat kernel (see: Sec. A.3) truncated at $L_{\text{max}} = 50$ spherical harmonics. The diffusion-time used in the analytic kernel is set to $t_{\text{analytical}} \approx 0.25$ to match the diffusion length observed on the discretized graph (and account for the number of nodes N).

Ellipsoid: We embed an ellipsoid $\frac{x^2}{a^2} + \frac{y^2}{b^2} + \frac{z^2}{c^2} = 1$ in \mathbb{R}^3 (with $a = 1.0, b = 1.3, c = 0.7$) and discretize it via scaled Fibonacci construction. As a reference kernel, we use the graph heat kernel $\mathbf{K}_{\text{true}} = \exp(-t\mathbf{L})$ computed from a k NN graph Laplacian on the ellipsoid.

Möbius strip: We embed a Möbius strip in \mathbb{R}^3 and discretize it using a uniform grid in the intrinsic parameters (u, v) . The ground truth is constructed similarly as for the ellipsoid. The Möbius strip is in principle more sensitive to discretization and graph construction (e.g., near-duplicate points, irregular sampling density, or disconnected k NN graphs can destabilize training).

Table 1. Summary of results for each manifold. Mean and median (clamped) absolute relative error (RE) and mean squared error values are computed across all validation nodes. ‘‘Time’’ refers to mean kernel evaluation time on 512 out-of-sample manifold points (in seconds); Spectral Time refers to the time taken by the baseline spectral decomposition method.

Manifold	R^2	Mean RE	Median RE	MSE	MRFs Time	Spectral Time	Speed-up
Sphere	0.997	0.23	0.12	26.9	$0.066 \pm 3.3 \times 10^{-5}$	$3.41 \pm 3.1 \times 10^{-5}$	55.2
Ellipsoid	0.995	0.37	0.18	46.7	$0.058 \pm 2.0 \times 10^{-5}$	$3.59 \pm 1.7 \times 10^{-5}$	61.2
Möbius strip	0.997	0.11	0.08	17.9	$0.059 \pm 2.3 \times 10^{-5}$	$2.14 \pm 1.7 \times 10^{-5}$	37.2
Torus	0.983	0.44	0.21	115.7	$0.061 \pm 2.9 \times 10^{-5}$	$3.62 \pm 3.1 \times 10^{-5}$	58.1

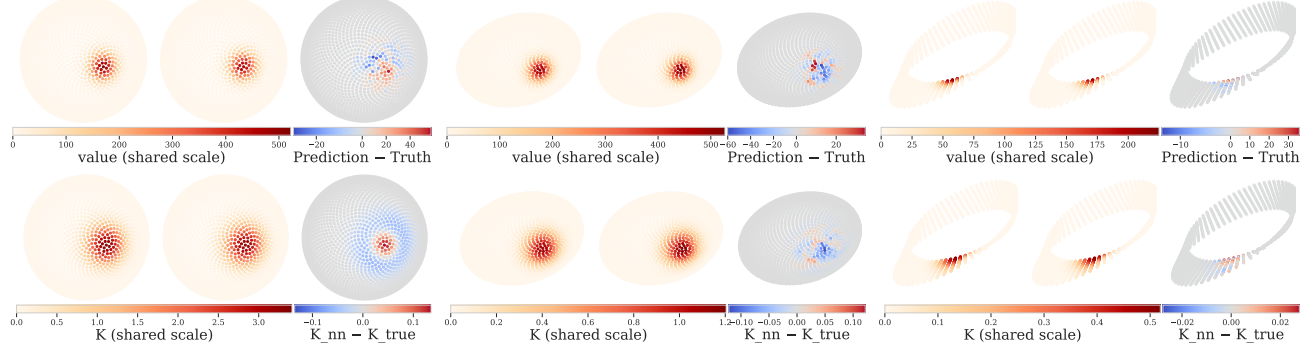


Figure 4. Qualitative field and heat kernel comparisons for a sphere (left), an ellipsoid (middle), and a Möbius strip (right). Example validation start (top row): predicted $g_\theta(\mathbf{x}, \cdot)$, ground truth $\phi_f(\mathbf{x})[\cdot]$, and residual $g_\theta(\mathbf{x}, \cdot) - \phi_f(\mathbf{x})[\cdot]$ on the geometry. Reference graph heat kernel (bottom row) $K^{\text{heat}}(\mathbf{x}, \cdot)$ compared to Frobenius-aligned induced kernel $\tilde{K}_\theta(\mathbf{x}, \cdot) = \tilde{K}_{\text{NN}}(\mathbf{x}, \cdot)$, and their difference, for a representative start point.

3.2.1. RESULTS

For all considered manifolds, the 3D field plots confirm that the learned predictor reproduces the localized, structured heat profile (for a sphere, radially symmetric) and that residuals are concentrated near the peak (Fig. 4). After Frobenius alignment, the induced kernel matrix \mathbf{K}_θ matches the analytic kernel matrix, with remaining error again localized near the center. Validation scatter plots show strong monotonic agreement with the ground truth values, with the largest deviations at the highest-intensity region near the source point where the field is most sharply peaked. Detailed results for the torus are in the Appendix (Sec. A.6; the same conclusions as for other shapes). All the results are summarized in Table 1. Importantly, MRFs offer significant speedups over the brute-force approaches, from **37x** to **61x+** in inference.

3.3. Interpolation on Meshes

As a downstream application for MRFs, we choose the task of interpolating various fields defined on meshes representing rigid and deformable objects. Experiments were run using a TPU v6e and an A100 GPU (for neural network training only).

Vertex normal prediction: Here we focus on predicting normal vectors in the vertices of the mesh representing

rigid body. Given a mesh G with vertex set V and vertex positions $\{\mathbf{x}_i \in \mathbb{R}^3\}_{i \in V}$, let $\{\mathbf{n}_i \in \mathbb{R}^3\}_{i \in V}$ denote the unit vertex normals computed from incident faces. We randomly mask a subset $M \subseteq V$ of size $|M| = 0.8|V|$ (80% missing normals), set masked normals to zero, and predict normals at masked vertices using kernel-based field integration on G . Our experiments use meshes from the Thingi10k dataset (Zhou & Jacobson, 2016). We compare the performance of our MRF approach against the baseline method of explicitly forming the full heat kernel matrix using spectral computations (see Appendix A.7 for more details).

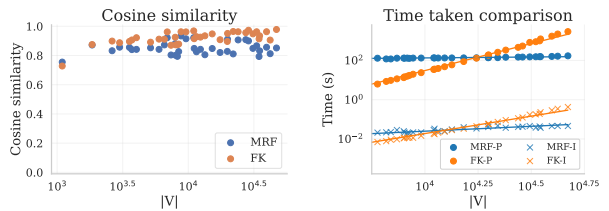


Figure 5. MRFs vs full kernel (FK) construction for vertex normal prediction; preprocessing and interpolation times are denoted by ‘‘-P’’ and ‘‘-I’’, respectively.

Fig. 5 shows that the baseline kernel construction cost grows rapidly with $|V|$, whereas the MRFs preprocessing time is

comparatively stable due to using fixed walk/training budgets. In our largest completed run ($|V| = 47,024$), kernel construction took 2936sec while MRF data generation and training took 171sec; baseline interpolation took 0.42sec while MRFs took 0.45sec. This gap widens further for larger meshes as explicitly storing $K \in \mathbb{R}^{|V| \times |V|}$ requires $O(|V|^2)$ memory, making full kernel formation intractable beyond 10^5 vertices. The MRF approach remains accurate compared with baseline. We conclude that MRFs can approximate the full kernel interpolant with comparable cosine similarity, while offering a more scalable inference path on meshes where explicit kernel construction is impractical.

Velocity prediction: We also evaluate interpolation on the `flag_simple` dataset (Pfaff et al., 2020) where the signal of interest is the per-node velocity field. For a given mesh with node set V and node positions $\{\mathbf{x}_i \in \mathbb{R}^3\}_{i \in V}$, let $\{\mathbf{u}_i \in \mathbb{R}^3\}_{i \in V}$ denote the ground truth velocity vectors at a fixed time step. We randomly mask a small subset $M \subseteq V$ with $|M| = 0.05|V|$ (5% missing velocities), set $u_i = 0$ for $i \in M$, and predict velocities at masked nodes using heat-kernel field integration (setup as in (Choromanski et al., 2023)).

The `flag_simple` meshes have only $\approx 1.5k$ vertices, which can be too small to expose inference-time scaling trends. To probe larger problem sizes, we construct a denser node set \tilde{V} by sampling additional points on triangle faces, using area-weighted barycentric sampling. The mesh surface is represented by a set of triangular faces. Concretely, for a target size $|\tilde{V}| = n_{\text{dense}}$, we draw $n_{\text{dense}} - |V|$ faces i.i.d. (with probability proportional to triangle area). For each sampled face, we draw barycentric weights $(\beta_0, \beta_1, \beta_2)$ (uniform on the 2-simplex) and define the sampled point's position as a convex combination of the triangle's three incident vertex positions. At each time step, we assign a velocity to each sampled point by applying the same barycentric weights to the velocities of the corresponding face vertices, yielding a dense velocity field $\mathbf{U} \in \mathbb{R}^{|\tilde{V}| \times 3}$.

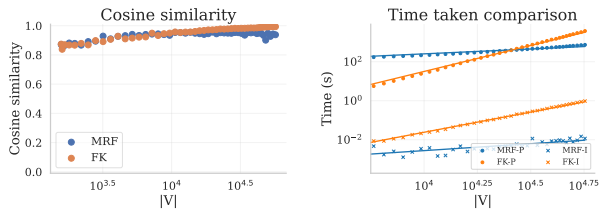


Figure 6. Velocity prediction on `flag_simple` under mesh densification. Setting analogous to the one in Fig. 5.

We then build a sparse graph on \tilde{V} (using the reference geometry from the first evaluated frame) via a k NN construction in \mathbb{R}^3 and define a symmetric, normalized affinity matrix $\mathbf{W}_f := \mathbf{D}^{-1/2} \mathbf{W} \mathbf{D}^{-1/2}$ where \mathbf{W} has Gaus-

sian weights $W_{ij} = \exp(-\|\mathbf{x}_i - \mathbf{x}_j\|_2^2/\sigma^2)$ and \mathbf{D} is the degree matrix of \mathbf{W} . The corresponding heat kernel is $\mathbf{K} = \exp(\tau \mathbf{W}_f)$.

Figure 6 shows that the dense spectral baseline exhibits the expected steep growth in preprocessing time, while MRF preprocessing remains comparatively stable across the tested range since training/feature budgets are fixed per discretization. At inference time, MRFs consistently outperform the baseline, with speedups that grow greater than 10x as n_{dense} increases.

4. Positivity & Boundedness of MRFs and General Bi-variate Functions

Note that GRFs, by definition (see: Algorithm 1), provide positive random features. Furthermore, our NNs (using GRFs as teachers) are forced to produce such features (via inference-time clamping). Their boundedness follows from the fact that, in our applications (see: Sec. 3), the considered NNs are continuous functions defined on compact manifolds. As mentioned before, both properties (positivity & boundedness) play an important role in getting accurate estimators.

As we already discussed in Sec. 2, general bi-variate functions F can be handled by MRFs via standard ML regression methods used to fit F to formula from Eq. 4. We also would like to emphasize that matrices \mathbf{W} used there can be thought of as “generalized” weighted adjacency matrices, obtained from original weighted adjacency matrices via various transformations (e.g. degree-based normalization), as discussed in (Reid et al., 2024b). Thus in this paper we focused on the (already rich) family of functions defined by Eq. 4.

5. Conclusion

We have presented a new paradigm of *Manifold Random Features* (MRFs), designed for scalable computations involving bi-variate functions operating on manifolds. MRFs are built with the use of Graph Random Features (GRFs), operating on the discretized manifolds. GRFs are used as teachers for the supervised learning of the continuous fields encoding the MRF-mechanisms. We provide strong empirical validation of MRFs, complemented with rigorous mathematical analysis. As a byproduct of our analysis, we show deep connection between combinatorial concepts of random walks on graphs representing discretized manifolds and continuous kernel functions on these manifolds, in particular by re-discovering recently proposed new class of estimators approximating Gaussian kernels with positive and bounded random features.

Impact Statement

This paper presents work whose goal is to advance the field of Machine Learning. There are many potential societal consequences of our work, none of which we feel must be specifically highlighted here. We do believe that this work might lead to the discovery of new mechanisms of random features operating in continuous spaces and encoded as neural networks that are trained with the supervision provided by Graph Random Features teachers.

References

Brandolini, L., Choirat, C., Colzani, L., Gigante, G., Seri, R., and Travagliini, G. Quadrature rules and distribution of points on manifolds, 2010. URL <https://arxiv.org/abs/1012.5409>.

Cadavid, C. A., Hoyos, P., Jorgenson, J., Smajlović, L., and Vélez, J. D. On an approach for evaluating certain trigonometric character sums using the discrete time heat kernel, 2022. URL <https://arxiv.org/abs/2201.07878>.

Choromanski, K. and Sindhwan, V. Recycling randomness with structure for sublinear time kernel expansions. In Balcan, M. and Weinberger, K. Q. (eds.), *Proceedings of the 33nd International Conference on Machine Learning, ICML 2016, New York City, NY, USA, June 19-24, 2016*, volume 48 of *JMLR Workshop and Conference Proceedings*, pp. 2502–2510. JMLR.org, 2016. URL <http://proceedings.mlr.press/v48/choromanski16.html>.

Choromanski, K., Rowland, M., Chen, W., and Weller, A. Unifying orthogonal monte carlo methods. In Chaudhuri, K. and Salakhutdinov, R. (eds.), *Proceedings of the 36th International Conference on Machine Learning, ICML 2019, 9-15 June 2019, Long Beach, California, USA*, volume 97 of *Proceedings of Machine Learning Research*, pp. 1203–1212. PMLR, 2019. URL <http://proceedings.mlr.press/v97/choromanski19a.html>.

Choromanski, K., Dubey, A., Sehanobish, A., and Reid, I. Computationally-efficient graph modeling with refined graph random features. *CoRR*, abs/2510.07716, 2025. doi: 10.48550/ARXIV.2510.07716. URL <https://doi.org/10.48550/arXiv.2510.07716>.

Choromanski, K. M. Taming graph kernels with random features. In Krause, A., Brunskill, E., Cho, K., Engelhardt, B., Sabato, S., and Scarlett, J. (eds.), *International Conference on Machine Learning, ICML 2023, 23-29 July 2023, Honolulu, Hawaii, USA*, volume 202 of *Proceedings of Machine Learning Research*, pp. 5964–5977. PMLR, 2023. URL <https://proceedings.mlr.press/v202/choromanski23a.html>.

Choromanski, K. M., Rowland, M., and Weller, A. The unreasonable effectiveness of structured random orthogonal embeddings. In Guyon, I., von Luxburg, U., Bengio, S., Wallach, H. M., Fergus, R., Vishwanathan, S. V. N., and Garnett, R. (eds.), *Advances in Neural Information Processing Systems 30: Annual Conference on Neural Information Processing Systems 2017, December 4-9, 2017, Long Beach, CA, USA*, pp. 219–228, 2017.

Choromanski, K. M., Likhosherstov, V., Dohan, D., Song, X., Gane, A., Sarlós, T., Hawkins, P., Davis, J. Q., Mohiuddin, A., Kaiser, L., Belanger, D. B., Colwell, L. J., and Weller, A. Rethinking attention with performers. In *9th International Conference on Learning Representations, ICLR 2021, Virtual Event, Austria, May 3-7, 2021*. OpenReview.net, 2021. URL <https://openreview.net/forum?id=Ua6zuk0WRH>.

Choromanski, K. M., Lin, H., Chen, H., Sehanobish, A., Ma, Y., Jain, D., Varley, J., Zeng, A., Ryoo, M. S., Likhosherstov, V., Kalashnikov, D., Sindhwan, V., and Weller, A. Hybrid random features. In *The Tenth International Conference on Learning Representations, ICLR 2022, Virtual Event, April 25-29, 2022*. OpenReview.net, 2022. URL <https://openreview.net/forum?id=EMigfE6ZeS>.

Choromanski, K. M., Sehanobish, A., Lin, H., Zhao, Y., Berger, E., Parshakova, T., Pan, A., Watkins, D., Zhang, T., Likhosherstov, V., Basu Roy Chowdhury, S., Dubey, K. A., Jain, D., Sarlos, T., Chaturvedi, S., and Weller, A. Efficient graph field integrators meet point clouds. In Krause, A., Brunskill, E., Cho, K., Engelhardt, B., Sabato, S., and Scarlett, J. (eds.), *Proceedings of the 40th International Conference on Machine Learning*, volume 202 of *Proceedings of Machine Learning Research*, pp. 5978–6004. PMLR, 23–29 Jul 2023. URL <https://proceedings.mlr.press/v202/choromanski23b.html>.

Dasgupta, S. and Gupta, A. An elementary proof of a theorem of johnson and lindenstrauss. *Random Struct. Algorithms*, 22(1):60–65, 2003. doi: 10.1002/RSA.10073. URL <https://doi.org/10.1002/rsa.10073>.

Grigor'yan, A. *Heat Kernel and Analysis on Manifolds*, volume 47 of *AMS/IP Studies in Advanced Mathematics*. American Mathematical Society, 2009.

Huang, P., Avron, H., Sainath, T. N., Sindhwan, V., and Ramabhadran, B. Kernel methods match deep neural networks on TIMIT. In *IEEE International Conference on Acoustics, Speech and Signal Processing, ICASSP 2014, Florence, Italy, May 4-9, 2014*, pp. 205–209. IEEE, 2014.

doi: 10.1109/ICASSP.2014.6853587. URL <https://doi.org/10.1109/ICASSP.2014.6853587>.

Kim, S. M., Kim, B., Sehanobish, A., Choromanski, K., Shim, D., Dubey, A., and hwan Oh, M. Magnitude layers for implicit neural representations in 3d, 2024. URL <https://arxiv.org/abs/2410.09771>.

Le, Q. V., Sarlós, T., and Smola, A. J. Fastfood - computing hilbert space expansions in loglinear time. In *Proceedings of the 30th International Conference on Machine Learning, ICML 2013, Atlanta, GA, USA, 16-21 June 2013*, volume 28 of *JMLR Workshop and Conference Proceedings*, pp. 244–252. JMLR.org, 2013. URL <http://proceedings.mlr.press/v28/le13.html>.

Likhosherstov, V., Choromanski, K. M., Davis, J. Q., Song, X., and Weller, A. Sub-linear memory: How to make performers slim. In Ranzato, M., Beygelzimer, A., Dauphin, Y. N., Liang, P., and Vaughan, J. W. (eds.), *Advances in Neural Information Processing Systems 34: Annual Conference on Neural Information Processing Systems 2021, NeurIPS 2021, December 6-14, 2021, virtual*, pp. 6707–6719, 2021.

Likhosherstov, V., Choromanski, K. M., Dubey, K. A., Liu, F., Sarlós, T., and Weller, A. Chefs' random tables: Non-trigonometric random features. In Koyejo, S., Mohamed, S., Agarwal, A., Belgrave, D., Cho, K., and Oh, A. (eds.), *Advances in Neural Information Processing Systems 35: Annual Conference on Neural Information Processing Systems 2022, NeurIPS 2022, New Orleans, LA, USA, November 28 - December 9, 2022*, 2022.

Likhosherstov, V., Choromanski, K. M., Dubey, K. A., Liu, F., Sarlós, T., and Weller, A. Dense-exponential random features: Sharp positive estimators of the gaussian kernel. In Oh, A., Naumann, T., Globerson, A., Saenko, K., Hardt, M., and Levine, S. (eds.), *Advances in Neural Information Processing Systems 36: Annual Conference on Neural Information Processing Systems 2023, NeurIPS 2023, New Orleans, LA, USA, December 10 - 16, 2023*, 2023.

Liu, F., Huang, X., Chen, Y., and Suykens, J. A. K. Random features for kernel approximation: A survey on algorithms, theory, and beyond. *IEEE Trans. Pattern Anal. Mach. Intell.*, 44(10):7128–7148, 2022. doi: 10.1109/TPAMI.2021.3097011. URL <https://doi.org/10.1109/TPAMI.2021.3097011>.

Nguyen, D., Joshi, A., and Salim, F. D. Spectraformer: A unified random feature framework for transformer. *CoRR*, abs/2405.15310, 2024. doi: 10.48550/ARXIV.2405.15310. URL <https://doi.org/10.48550/arXiv.2405.15310>.

Peng, H., Pappas, N., Yogatama, D., Schwartz, R., Smith, N. A., and Kong, L. Random feature attention. In *9th International Conference on Learning Representations, ICLR 2021, Virtual Event, Austria, May 3-7, 2021*. OpenReview.net, 2021. URL <https://openreview.net/forum?id=QtTKTdVrFBB>.

Pfaff, T., Fortunato, M., Sanchez-Gonzalez, A., and Battaglia, P. W. Learning mesh-based simulation with graph networks. *CoRR*, abs/2010.03409, 2020. URL <https://arxiv.org/abs/2010.03409>.

Pham, N. and Pagh, R. Tensor sketch: Fast and scalable polynomial kernel approximation. *CoRR*, abs/2505.08146, 2025. doi: 10.48550/ARXIV.2505.08146. URL <https://doi.org/10.48550/arXiv.2505.08146>.

Rahimi, A. and Recht, B. Random features for large-scale kernel machines. In Platt, J. C., Koller, D., Singer, Y., and Roweis, S. T. (eds.), *Advances in Neural Information Processing Systems 20, Proceedings of the Twenty-First Annual Conference on Neural Information Processing Systems, Vancouver, British Columbia, Canada, December 3-6, 2007*, pp. 1177–1184. Curran Associates, Inc., 2007.

Rahimi, A. and Recht, B. Weighted sums of random kitchen sinks: Replacing minimization with randomization in learning. In Koller, D., Schuurmans, D., Bengio, Y., and Bottou, L. (eds.), *Advances in Neural Information Processing Systems 21, Proceedings of the Twenty-Second Annual Conference on Neural Information Processing Systems, Vancouver, British Columbia, Canada, December 8-11, 2008*, pp. 1313–1320. Curran Associates, Inc., 2008.

Reid, I., Berger, E., Choromanski, K. M., and Weller, A. Repelling random walks. In *The Twelfth International Conference on Learning Representations, ICLR 2024, Vienna, Austria, May 7-11, 2024*. OpenReview.net, 2024a. URL <https://openreview.net/forum?id=31I0mrnoP4>.

Reid, I., Choromanski, K. M., Berger, E., and Weller, A. General graph random features. In *The Twelfth International Conference on Learning Representations, ICLR 2024, Vienna, Austria, May 7-11, 2024*. OpenReview.net, 2024b. URL <https://openreview.net/forum?id=viftsX50Rt>.

Rowland, M., Choromanski, K., Chalus, F., Pacchiano, A., Sarlós, T., Turner, R. E., and Weller, A. Geometrically coupled monte carlo sampling. In Bengio, S., Wallach, H. M., Larochelle, H., Grauman, K., Cesa-Bianchi, N., and Garnett, R. (eds.), *Advances in Neural Information Processing Systems 31: Annual Conference on Neural*

Information Processing Systems 2018, NeurIPS 2018, December 3-8, 2018, Montréal, Canada, pp. 195–205, 2018.

Sehanobish, A., Choromanski, K. M., Zhao, Y., Dubey, K. A., and Likhosherstov, V. Scalable neural network kernels. In *The Twelfth International Conference on Learning Representations, ICLR 2024, Vienna, Austria, May 7-11, 2024*. OpenReview.net, 2024. URL <https://openreview.net/forum?id=4iPw1k1FWa>.

Solomon, J., Crane, K., and Vouga, E. Laplace-beltrami: The swiss army knife of geometry processing. *Symposium on Geometry Processing*, 2014. URL <http://ddg.cs.columbia.edu/SGP2014/LaplaceBeltrami.pdf>.

Sun, Y., Gilbert, A. C., and Tewari, A. But how does it work in theory? linear SVM with random features. In Bengio, S., Wallach, H. M., Larochelle, H., Grauman, K., Cesa-Bianchi, N., and Garnett, R. (eds.), *Advances in Neural Information Processing Systems 31: Annual Conference on Neural Information Processing Systems 2018, NeurIPS 2018, December 3-8, 2018, Montréal, Canada*, pp. 3383–3392, 2018.

Sun, Y., Li, Z., Zhang, Y., Pan, T., Dong, B., Guo, Y., and Wang, J. Efficient attention mechanisms for large language models: A survey. *CoRR*, abs/2507.19595, 2025. doi: 10.48550/ARXIV.2507.19595. URL <https://doi.org/10.48550/arXiv.2507.19595>.

Yang, J., Sindhwani, V., Avron, H., and Mahoney, M. W. Quasi-monte carlo feature maps for shift-invariant kernels. In *Proceedings of the 31th International Conference on Machine Learning, ICML 2014, Beijing, China, 21-26 June 2014*, volume 32 of *JMLR Workshop and Conference Proceedings*, pp. 485–493. JMLR.org, 2014. URL <http://proceedings.mlr.press/v32/yangb14.html>.

Yu, F. X., Suresh, A. T., Choromanski, K. M., Holtmann-Rice, D. N., and Kumar, S. Orthogonal random features. In Lee, D. D., Sugiyama, M., von Luxburg, U., Guyon, I., and Garnett, R. (eds.), *Advances in Neural Information Processing Systems 29: Annual Conference on Neural Information Processing Systems 2016, December 5-10, 2016, Barcelona, Spain*, pp. 1975–1983, 2016.

Zhang, M., Bhatia, K., Kumbong, H., and Ré, C. The hedgehog & the porcupine: Expressive linear attention with softmax mimicry. In *The Twelfth International Conference on Learning Representations, ICLR 2024, Vienna, Austria, May 7-11, 2024*. OpenReview.net, 2024. URL <https://openreview.net/forum?id=4g0212N2Nx>.

Zhang, M., Lin, J. A., Choromanski, K., Weller, A., Turner, R. E., and Reid, I. Graph random features for scalable gaussian processes. *CoRR*, abs/2509.03691, 2025. doi: 10.48550/ARXIV.2509.03691. URL <https://doi.org/10.48550/arXiv.2509.03691>.

Zhao, C. and Song, J. S. Exact heat kernel on a hypersphere and its applications in kernel svm. *Frontiers in Applied Mathematics and Statistics*, 4, January 2018. ISSN 2297-4687. doi: 10.3389/fams.2018.00001. URL <http://dx.doi.org/10.3389/fams.2018.00001>.

Zhou, Q. and Jacobson, A. Thingi10k: A dataset of 10,000 3d-printing models. *CoRR*, abs/1605.04797, 2016. URL <http://arxiv.org/abs/1605.04797>.

A. Appendix

A.1. Diffusion Kernel on Discrete Euclidean Grid

Let $d \in \mathbb{N}$ and, for each $n \in \mathbb{N}$, let $h_n := \frac{1}{n}$. Let \mathbb{T}^d be the d -dimensional torus and let $V_n \subset \mathbb{T}^d$ be the regular d -dimensional grid

$$V_n := \left\{ x = (k_1 h_n, \dots, k_d h_n) : k_j \in \{0, \dots, n-1\} \right\}.$$

Consider the graph whose vertices are V_n and whose neighbors are the $2d$ wrap-around nearest neighbors.

Theorem A.1 (Convergence of Discrete to Continuous Laplacian). *Define the averaging operator $\mathbf{T}_n : \mathbb{R}^{V_n} \rightarrow \mathbb{R}^{V_n}$ by*

$$(\mathbf{T}_n f)(x) := \frac{1}{2d} \sum_{y \sim x} f(y),$$

where the sum is over the $2d$ neighbors y of x in the wrap-around grid. Furthermore, denote the (random-walk) graph and rescaled Laplacian as

$$\mathbf{L}_{\text{curr}}^{(n)} := \mathbf{I} - \mathbf{T}_n \quad \mathbf{L}_n := \frac{2d}{h_n^2} \mathbf{L}_{\text{curr}}^{(n)} = \frac{2d}{h_n^2} (\mathbf{I} - \mathbf{T}_n).$$

Let Δ be the usual Laplacian on \mathbb{T}^d . Then we have

$$\mathbf{L}_n \xrightarrow{n \rightarrow \infty} -\Delta. \quad (19)$$

Proof. For $f \in C^4(\mathbb{T}^d)$ define its restriction to the grid V_n by $f_n(x) := f(x)$, $x \in V_n$. Fix $x \in \mathbb{T}^d$ and $f \in C^4(\mathbb{T}^d)$. For each coordinate direction \mathbf{e}_k ($k = 1, \dots, d$), we have the Taylor expansions

$$f(x \pm h_n \mathbf{e}_k) = f(x) \pm h_n \partial_k f(x) + \frac{h_n^2}{2} \partial_{kk} f(x) \pm \frac{h_n^3}{6} \partial_{kkk} f(\xi_{\pm}) + \frac{h_n^4}{24} \partial_{kkkk} f(\eta_{\pm}),$$

for some points ξ_{\pm}, η_{\pm} on the segment between x and $x \pm h_n \mathbf{e}_k$. Adding these two expansions gives

$$f(x + h_n \mathbf{e}_k) + f(x - h_n \mathbf{e}_k) = 2f(x) + h_n^2 \partial_{kk} f(x) + O(h_n^4).$$

Summing over $k = 1, \dots, d$,

$$\begin{aligned} \sum_{y \sim x} f(y) &= \sum_{k=1}^d (f(x + h_n \mathbf{e}_k) + f(x - h_n \mathbf{e}_k)) \\ &= \sum_{k=1}^d (2f(x) + h_n^2 \partial_{kk} f(x) + O(h_n^4)) \\ &= 2d f(x) + h_n^2 \sum_{k=1}^d \partial_{kk} f(x) + O(dh_n^4). \end{aligned}$$

Furthermore, we know

$$\begin{aligned} (\mathbf{L}_{\text{curr}}^{(n)} f_n)(x) &= f(x) - \frac{1}{2d} \sum_{y \sim x} f(y) \\ &= -\frac{h_n^2}{2d} \sum_{k=1}^d \partial_{kk} f(x) + O(h_n^4) \\ &= -\frac{h_n^2}{2d} \Delta f(x) + O(h_n^4), \end{aligned}$$

where we plugged in our earlier result in the second line. Multiplying by $\frac{2d}{h_n^2}$ gives

$$(\mathbf{L}_n f_n)(x) = \frac{2d}{h_n^2} (\mathbf{L}_{\text{curr}}^{(n)} f_n)(x) = -\Delta f(x) + O(h_n^2),$$

for any $x \in V_n$. Thus, for each smooth f ,

$$\mathbf{L}_n f_n \xrightarrow[n \rightarrow \infty]{} -\Delta f.$$

□

Theorem A.2 (Convergence of Discrete Diffusion Kernel to Periodized Gaussian). *Fix $\sigma > 0$ and let $f \in C^4(\mathbb{T}^d)$. Then we have*

$$\exp\left(-\frac{\sigma^2}{2}\mathbf{L}_n\right)f|_{V_n} \xrightarrow[n \rightarrow \infty]{} \left(\exp\left(\frac{\sigma^2}{2}\Delta\right)f\right)|_{V_n}.$$

Moreover, the limiting operator $\exp\left(\frac{\sigma^2}{2}\Delta\right)$ acts by convolution with a periodized Gaussian kernel

$$k_\sigma(x, y) = \sum_{k \in \mathbb{Z}^d} \frac{1}{(2\pi\sigma^2)^{d/2}} \exp\left(-\frac{\|x - y + k\|^2}{2\sigma^2}\right), \quad x, y \in \mathbb{T}^d.$$

Proof. Using the result of Theorem A.1 and exponentiating the operators implies that for any fixed $t \geq 0$,

$$e^{-t\mathbf{L}_n} f|_{V_n} \longrightarrow (e^{t\Delta} f)|_{V_n}.$$

Taking $t = \sigma^2/2$ yields the stated convergence.

The operator $e^{t\Delta}$ on the torus \mathbb{T}^d is the heat semigroup and admits an integral representation

$$(e^{t\Delta} f)(x) = \int_{\mathbb{T}^d} p_t(x, y) f(y) dy,$$

where p_t is the heat kernel on the torus. This kernel is obtained by periodizing the Euclidean heat kernel (Brandolini et al., 2010)

$$p_t(x, y) = \sum_{k \in \mathbb{Z}^d} \frac{1}{(4\pi t)^{d/2}} \exp\left(-\frac{\|x - y + k\|^2}{4t}\right).$$

Setting $t = \sigma^2/2$ gives

$$p_{\sigma^2/2}(x, y) = \sum_{k \in \mathbb{Z}^d} \frac{1}{(2\pi\sigma^2)^{d/2}} \exp\left(-\frac{\|x - y + k\|^2}{2\sigma^2}\right),$$

which is a Gaussian kernel with variance σ^2 in each coordinate, periodized to respect the torus geometry. □

Remark: If instead of the discrete grid, we worked on \mathbb{R}^d (no wrap-around), the corresponding kernel would be the standard Gaussian

$$K_\sigma(\mathbf{x}, \mathbf{y}) := \frac{1}{(2\pi\sigma^2)^{d/2}} \exp\left(-\frac{\|\mathbf{x} - \mathbf{y}\|^2}{2\sigma^2}\right),$$

which is the usual Gaussian kernel with bandwidth σ . On the torus we obtain its periodic version by summing over $k \in \mathbb{Z}^d$.

A.2. Euclidean Gaussian Feature Representation

Theorem A.3 (RBF Kernel Factorization). *Let $d \in \mathbb{N}$ and $\sigma > 0$, and define*

$$g_\sigma(\mathbf{x}, \boldsymbol{\omega}) := \left(\frac{2}{\pi\sigma^2}\right)^{d/4} \exp\left(-\frac{\|\mathbf{x} - \boldsymbol{\omega}\|^2}{\sigma^2}\right), \quad \mathbf{x}, \boldsymbol{\omega} \in \mathbb{R}^d.$$

Then for all $\mathbf{x}, \mathbf{y} \in \mathbb{R}^d$,

$$\int_{\mathbb{R}^d} g_\sigma(\mathbf{x}, \boldsymbol{\omega}) g_\sigma(\mathbf{y}, \boldsymbol{\omega}) d\boldsymbol{\omega} = \exp\left(-\frac{\|\mathbf{x} - \mathbf{y}\|^2}{2\sigma^2}\right).$$

In particular, g_σ is a continuous feature map for the Gaussian kernel with bandwidth σ .

Proof. Set $C_\sigma := \left(\frac{2}{\pi\sigma^2}\right)^{d/4}$ and $\mathbf{m} := \frac{\mathbf{x}+\mathbf{y}}{2}$ for fixed $\mathbf{x}, \mathbf{y} \in \mathbb{R}^d$. By Lemma A.4 we have

$$\|\mathbf{x} - \boldsymbol{\omega}\|^2 + \|\mathbf{y} - \boldsymbol{\omega}\|^2 = 2\|\boldsymbol{\omega} - \mathbf{m}\|^2 + \frac{1}{2}\|\mathbf{x} - \mathbf{y}\|^2.$$

Therefore,

$$\begin{aligned} \int_{\mathbb{R}^d} g_\sigma(\mathbf{x}, \boldsymbol{\omega}) g_\sigma(\mathbf{y}, \boldsymbol{\omega}) d\boldsymbol{\omega} &= C_\sigma^2 \int_{\mathbb{R}^d} \exp\left(-\frac{\|\mathbf{x} - \boldsymbol{\omega}\|^2}{\sigma^2} - \frac{\|\mathbf{y} - \boldsymbol{\omega}\|^2}{\sigma^2}\right) d\boldsymbol{\omega} \\ &= C_\sigma^2 \exp\left(-\frac{\|\mathbf{x} - \mathbf{y}\|^2}{2\sigma^2}\right) \int_{\mathbb{R}^d} \exp\left(-\frac{2\|\boldsymbol{\omega} - \mathbf{m}\|^2}{\sigma^2}\right) d\boldsymbol{\omega} \\ &= C_\sigma^2 \exp\left(-\frac{\|\mathbf{x} - \mathbf{y}\|^2}{2\sigma^2}\right) \left(\frac{\pi\sigma^2}{2}\right)^{d/2} \\ &= \exp\left(-\frac{\|\mathbf{x} - \mathbf{y}\|^2}{2\sigma^2}\right), \end{aligned}$$

noting that for $a > 0$, $\int_{\mathbb{R}} e^{-au^2} du = \sqrt{\frac{\pi}{a}}$. \square

Lemma A.4. For any \mathbf{x}, \mathbf{y} in \mathbb{R}^d let $\mathbf{m} := \frac{\mathbf{x}+\mathbf{y}}{2}$, then we have

$$\|\mathbf{x} - \boldsymbol{\omega}\|^2 + \|\mathbf{y} - \boldsymbol{\omega}\|^2 = 2\|\boldsymbol{\omega} - \mathbf{m}\|^2 + \frac{1}{2}\|\mathbf{x} - \mathbf{y}\|^2, \quad \boldsymbol{\omega} \in \mathbb{R}^d. \quad (20)$$

Proof. We have

$$\begin{aligned} \|\mathbf{x} - \boldsymbol{\omega}\|^2 + \|\mathbf{y} - \boldsymbol{\omega}\|^2 &= (\|\mathbf{x}\|^2 - 2\langle \mathbf{x}, \boldsymbol{\omega} \rangle + \|\boldsymbol{\omega}\|^2) + (\|\mathbf{y}\|^2 - 2\langle \mathbf{y}, \boldsymbol{\omega} \rangle + \|\boldsymbol{\omega}\|^2) \\ &= 2\|\boldsymbol{\omega}\|^2 - 2\langle \mathbf{x} + \mathbf{y}, \boldsymbol{\omega} \rangle + \|\mathbf{x}\|^2 + \|\mathbf{y}\|^2 \\ &= 2\left(\|\boldsymbol{\omega}\|^2 - \left\langle \mathbf{x} + \mathbf{y}, \boldsymbol{\omega} \right\rangle + \left\| \frac{\mathbf{x} + \mathbf{y}}{2} \right\|^2\right) + \|\mathbf{x}\|^2 + \|\mathbf{y}\|^2 - \frac{1}{2}\|\mathbf{x} + \mathbf{y}\|^2 \\ &= 2\|\boldsymbol{\omega} - \mathbf{m}\|^2 + \frac{1}{2}\|\mathbf{x} - \mathbf{y}\|^2. \end{aligned}$$

\square

A.3. Ground Truth Specialization to Spheres and the Case of S^2

For the unit hypersphere $S^d \subset \mathbb{R}^{d+1}$, the heat kernel admits an explicit spectral expansion in terms of Gegenbauer polynomials. Following Theorem 1 of Zhao & Song (2018), the exact hyperspherical heat kernel $G^{\text{ext}}(\mathbf{x}, \mathbf{y}; t)$ on S^{n-1} (with $n = d + 1$) can be written as the uniformly and absolutely convergent series

$$G^{\text{ext}}(\mathbf{x}, \mathbf{y}; t) = \sum_{\ell=0}^{\infty} e^{-\ell(\ell+n-2)t} \frac{2\ell+n-2}{n-2} \frac{1}{A_{S^{n-1}}} C_\ell^{\frac{n-2}{2}}(\mathbf{x} \cdot \mathbf{y}), \quad (21)$$

where C_ℓ^α denotes the Gegenbauer polynomial of order ℓ and index α , $\mathbf{x} \cdot \mathbf{y} \in [-1, 1]$, $t > 0$, and

$$A_{S^{n-1}} = \frac{2\pi^{\frac{n}{2}}}{\Gamma\left(\frac{n}{2}\right)}$$

is the surface area of S^{n-1} .

In the case $d = 2$ (so $n = 3$ and we are on S^2), we have $\alpha = \frac{n-2}{2} = \frac{1}{2}$, and the Gegenbauer polynomials reduce to Legendre polynomials via $C_\ell^{1/2}(z) = P_\ell(z)$. Therefore (21) specializes to the classical spherical expansion

$$G^{\text{ext}}(\mathbf{x}, \mathbf{y}; t) = \sum_{\ell=0}^{\infty} \frac{2\ell+1}{4\pi} e^{-\ell(\ell+1)t} P_\ell(\langle \mathbf{x}, \mathbf{y} \rangle). \quad (22)$$

For numerical ground truth, we truncate (22) at $\ell \leq L_{\max}$:

$$K_t^{\text{true}}(\mathbf{x}_i, \mathbf{x}_j) \approx \sum_{\ell=0}^{L_{\max}} \frac{2\ell+1}{4\pi} e^{-\ell(\ell+1)t} P_\ell(\langle \mathbf{x}_i, \mathbf{x}_j \rangle),$$

where L_{\max} is chosen so that the tail mass is negligible. In our experiments, we choose $L_{\max} = 50$.

A.4. Convergence of kernels induced by MRFs to the standard Gaussian kernel

We consider a setting from Sec. 3.1. For a representative grid point c (we choose the center $c = (\frac{1}{2}, \dots, \frac{1}{2})$), we visualize the field $\omega \mapsto \psi_n(c)[\omega]$ over V_n and compare it to the analytic feature $g_\sigma(c, \omega)$ evaluated on the same grid. As n increases, the discrete field becomes increasingly smooth and radially symmetric, approaching the shape of the Gaussian bump predicted by the theory (see Figure 7 below for the two-dimensional case).

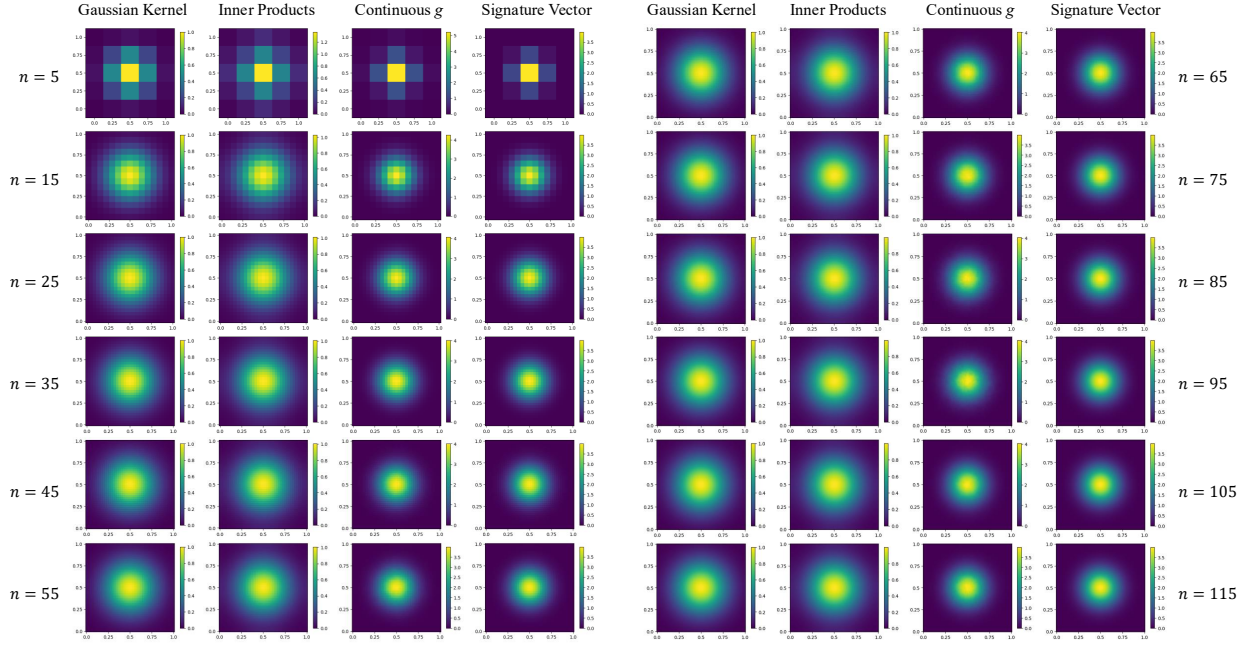


Figure 7. First column: Exact values of the Gaussian kernel, computed in the grid points and broadcast to all the points in the continuous rectangle corresponding to that grid point. **Second column:** Inner(dot)-products of the signature vectors, leading to the approximate Gaussian kernel values. **Third column:** The values of the exact function $g_\sigma(c, \omega)$ (for a fixed c), computed in the grid points and broadcast to all the points in the continuous rectangle corresponding to that grid point. **Fourth column:** Values of the renormalized signature vector $\psi(c)[\omega]$ for a fixed c . We use the following setting: $d = 2$, $\sigma = 0.2$, $p_{\text{halt}} = 0.005$, and $m = 100,000$.

A.5. Kernel reconstruction and scale alignment

In order to address the scaling challenge, as we go from the original continuous space to the discretized space, we conduct scale alignment that can be thought of as extra normalization. In matrix form, letting $\mathbf{G}_\theta \in \mathbb{R}^{N \times N}$ with $(\mathbf{G}_\theta)_{ij} = g_\theta(\mathbf{x}_i, \omega_j)$, the induced kernel is $\mathbf{K}_\theta = \mathbf{G}_\theta \mathbf{G}_\theta^\top$. To compare against a ground-truth kernel matrix \mathbf{K}_{GT} (see Sec. 2.2.1 for how these values are computed), we apply a single global scaling that matches Frobenius norms:

$$\tilde{\mathbf{K}}_\theta = \alpha \mathbf{K}_\theta, \quad \alpha = \frac{\|\mathbf{K}_{\text{GT}}\|_F}{\|\mathbf{K}_\theta\|_F}. \quad (23)$$

All kernel errors and visualizations use $\tilde{\mathbf{K}}_\theta$.

A.6. 2D Surfaces in 3D Spaces: Additional Results

A.6.1. TORUS

We embed a torus in \mathbb{R}^3 and discretize it using a uniform grid. We then proceed as for the sphere and ellipsoid case. The conclusions are the same as for the sphere and the ellipsoid (see: Fig. 8).

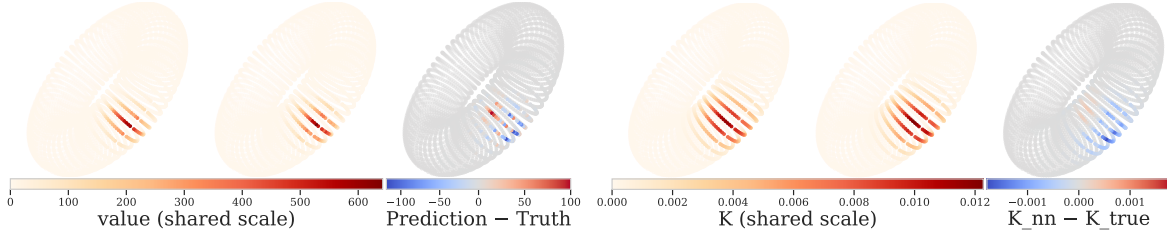


Figure 8. Qualitative field and heat kernel comparison for a torus. Example validation start (left): predicted $g_\theta(\mathbf{x}, \cdot)$, ground truth $\phi_f(\mathbf{x})[\cdot]$, and residual on the torus. Reference graph heat kernel (right) $K^{\text{heat}}(\mathbf{x}, \cdot)$ compared to Frobenius-aligned induced kernel $\tilde{K}_\theta(\mathbf{x}, \cdot) = \tilde{K}_{\text{NN}}(\mathbf{x}, \cdot)$, and their difference, for a representative start point.

A.6.2. VALIDATION DIAGNOSTICS FOR ALL SHAPES

Validation diagnostics results for all the shapes, confirming strong performance of the MRF method, are presented in Fig. 9, Fig. 10, Fig. 11 and Fig. 12.

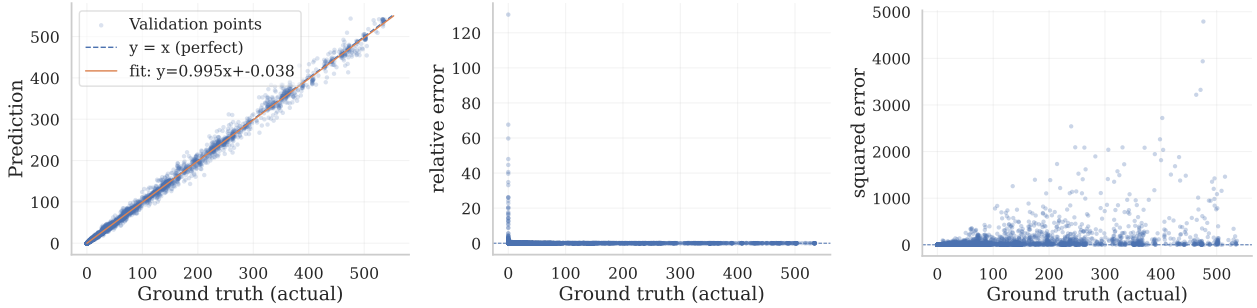


Figure 9. Sphere validation diagnostics. Left: predicted vs. ground-truth φ_t values. Middle/right: relative error and squared error as a function of ground-truth magnitude, highlighting where the model under/over-estimates.

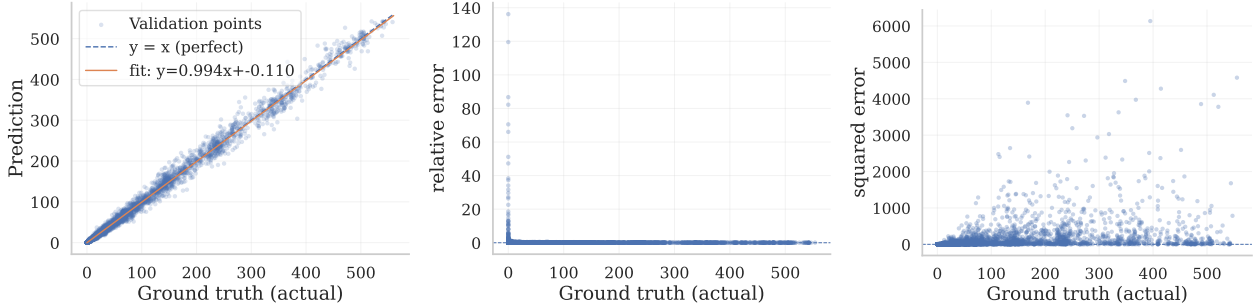


Figure 10. Ellipsoid validation diagnostics. Left: predicted vs. ground-truth φ_t values. Middle/right: relative and squared errors as a function of ground-truth magnitude.

A.7. Vertex Normal Prediction Set-up

We consider vertex normal interpolation on a triangular mesh with vertex set V , faces F , and vertex positions $\{\mathbf{x}_i \in \mathbb{R}^3\}_{i \in V}$. Ground-truth vertex normals $\{\mathbf{n}_i \in \mathbb{R}^3\}_{i \in V}$ are computed by accumulating incident (unnormalized) face normals and normalizing each vertex vector. We randomly mask a subset $M \subseteq V$ with $|M| = 0.8|V|$ (80% missing), set $\tilde{\mathbf{n}}_i = \mathbf{0}$ for $i \in M$ and $\tilde{\mathbf{n}}_i = \mathbf{n}_i$ otherwise, and predict normals at the masked vertices via kernel-based field integration. Performance is reported as the mean cosine similarity on the masked set, $\frac{1}{|M|} \sum_{i \in M} (\mathbf{n}_i^{\text{pred}})^\top \mathbf{n}_i$, where $\mathbf{n}_i^{\text{pred}}$ is the unit-normalized prediction. The mesh graph $G = (V, E)$ uses the mesh edges induced by faces. For each edge $(i, j) \in E$, we define an affinity

$$(\mathbf{W})_{ij} = \exp\left(-\frac{\|\mathbf{x}_i - \mathbf{x}_j\|^2}{\sigma^2}\right), \quad \sigma^2 = \text{median}_{(i,j) \in E} \|\mathbf{x}_i - \mathbf{x}_j\|^2,$$

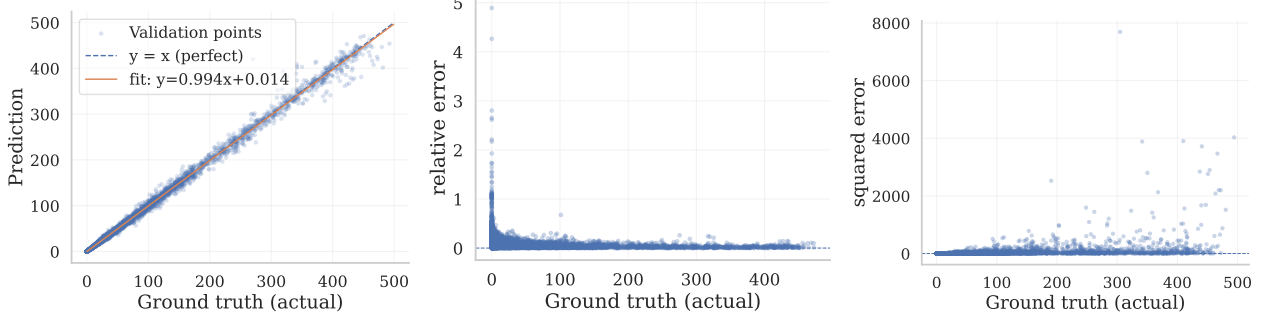


Figure 11. Möbius validation diagnostics. Predicted vs. ground-truth φ_t values (left) and error vs. truth (middle/right), illustrating calibration and where errors concentrate.

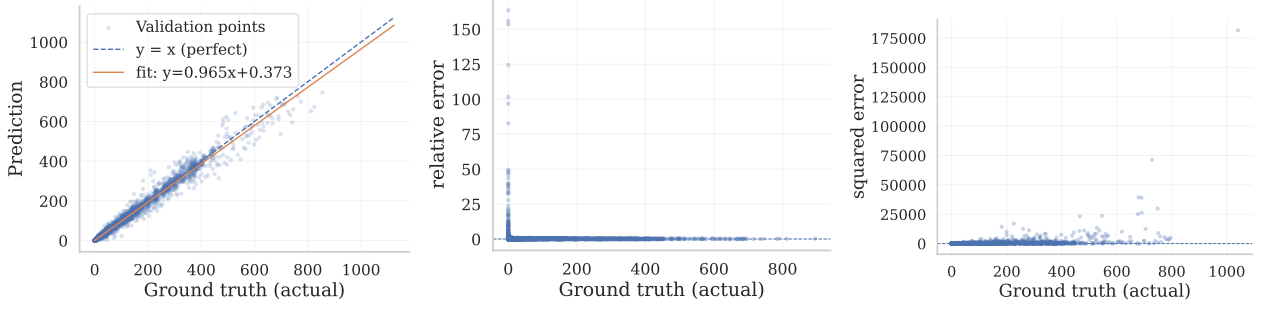


Figure 12. Torus validation diagnostics. Predicted vs. ground-truth φ_t values (left) and error vs. truth (middle/right), illustrating calibration and where errors concentrate.

compute degrees $(\mathbf{D})_{ii} = \sum_j (\mathbf{W})_{ij}$, and form the symmetrically-normalized matrix $\mathbf{W}_f = \mathbf{D}^{-1/2} \mathbf{W} \mathbf{D}^{-1/2}$. The full-kernel (FK) baseline explicitly constructs the dense kernel $\mathbf{K} = \exp(\tau \mathbf{W}_f)$, with $\tau = 20$, by eigen-decomposition of the dense \mathbf{W}_f (double precision) and then applies $\mathbf{N}^{\text{pred}} = \mathbf{K} \tilde{\mathbf{N}}$ with $\tilde{\mathbf{N}} \in \mathbb{R}^{|V| \times 3}$ the masked normal field (masked rows set to $\mathbf{0}$), followed by row-wise unit normalization. We record FK preprocessing time as dense \mathbf{W}_f construction plus eigendecomposition and kernel formation, and FK interpolation time as the matrix–field product $\mathbf{K} \tilde{\mathbf{N}}$ plus normalization.

MRFs targets the same kernel $\mathbf{K} = \exp(\tau \mathbf{W}_f)$ but avoids explicit construction by learning a low-rank factorization. We first estimate signature values corresponding to $\exp(\frac{\tau}{2} \mathbf{W}_f)$ using the g-GRF random-walk estimator with modulation coefficients $\alpha_k = (\frac{\tau}{2})^k / k!$ (truncated when $\alpha_k < 10^{-300}$), halting probability $p_{\text{halt}} = 0.01$, and $m = 10,000$ walks per start node. We sample 1000 start nodes uniformly without replacement (restricted to vertices when a denser discretization is used). For each start, we sample candidate anchors ω uniformly, keep all samples with target value at least 0.1, and retain smaller targets with probability 0.025. We also train a continuous surrogate $g_\theta(\mathbf{x}_{\text{start}}, \mathbf{x}_\omega)$ using a 3-layer MLP with two 128-wide ReLU hidden layers. Optimization uses Adam with learning rate 10^{-3} , batch size 32,768, 1000 epochs, a relative-error loss with $\varepsilon = 0.1$, and a 20% validation split.

For training g_θ we use a denser point set on the surface: by default we set $N_{\text{dense}} = \max(|V|, 5000)$ by adding area-weighted samples on faces and build a $k\text{NN}$ graph on these points with $k = 16$. Inference remains on the original vertices: we sample $n_{\text{rf}} = 256$ anchors $\{\omega_\ell\}$ uniformly from the dense set and approximate \mathbf{K} via $\mathbf{K} \approx \Phi \Phi^\top$ with $(\Phi)_{i\ell} = g_\theta(\mathbf{x}_i, \mathbf{x}_{\omega_\ell}, d(i, \omega_\ell)) / \sqrt{n_{\text{rf}}}$, applying $\mathbf{N}^{\text{pred}} \approx \Phi(\Phi^\top \tilde{\mathbf{N}})$ and normalizing row-wise. MRF preprocessing time includes supervision generation and training, and MRF interpolation time includes anchor sampling, distance computation, network evaluation, and accumulation. We evaluate on meshes from Thingi10k with the following mesh IDs:

[368622, 42435, 65282, 116878, 409624, 101902, 73410, 87602, 255172, 98480, 57140, 285606, 96123, 203289, 87601, 409629, 37384, 57084, 136024, 202267, 101619, 72896, 90064, 127243, 78671, 285610, 75667, 80597, 75651, 75654, 75657, 75665, 75652, 123472, 88855, 444375, 208741, 73877]

A.7.1. MORE DETAILS REGARDING VELOCITY PREDICTION SETUP

Since velocity magnitudes are meaningful (unlike unit normals), we use a normalized kernel interpolant. Let $\mathbf{m} \in \{0, 1\}^{|\tilde{V}|}$ be the indicator of observed nodes ($m_i = 1$ if $i \in M$, else 0), and let $\mathbf{m} \odot \mathbf{U}$ denote row-wise masking. We predict the full field via normalization:

$$\mathbf{U}^{\text{pred}} = \frac{\mathbf{K}(\mathbf{m} \odot \mathbf{U})}{\mathbf{K}\mathbf{m}}, \quad (24)$$

where the division is row-wise and applied to each of the 3 velocity channels.

To match the full-kernel baseline used in vertex-normal prediction, we compute \mathbf{K} via a full spectral decomposition. Specifically, we form \mathbf{W}_f and compute $\mathbf{W}_f = \mathbf{V} \text{diag}(\boldsymbol{\lambda}) \mathbf{V}^\top$, so that $\mathbf{K} = \mathbf{V} \text{diag}(\exp(\tau\boldsymbol{\lambda})) \mathbf{V}^\top$. Baseline preprocessing time therefore includes graph construction and the dense eigendecomposition (dominated by $O(|\tilde{V}|^3)$ time and $O(|\tilde{V}|^2)$ memory to store \mathbf{V}), and each per-frame interpolation requires two dense applications of \mathbf{K} (we apply \mathbf{K} once to the stacked right-hand side $[\mathbf{m}, \mathbf{m} \odot \mathbf{U}]$ to obtain both numerator and denominator).

For MRFs, we train the regressor g_θ once per discretization on the same dense graph, and precompute a random-feature matrix $\mathbf{Z} \in \mathbb{R}^{|\tilde{V}| \times M}$ for a fixed number of features M . This yields the approximation $\mathbf{K} \approx \mathbf{Z}\mathbf{Z}^\top$, so that per-frame interpolation reduces to two thin matrix multiplications: $\mathbf{Z}\mathbf{Z}^\top(\mathbf{m} \odot \mathbf{U}) = \mathbf{Z}(\mathbf{Z}^\top(\mathbf{m} \odot \mathbf{U}))$ and similarly for $\mathbf{K}\mathbf{m}$. We report MRF preprocessing as supervision generation, training, and feature precomputation, and MRF interpolation time as the rest.

Code for all our experiments can be found [here](#).